



KCl flux-induced growth of isometric crystals of cadmium-containing early transition-metal (Ti^{4+} , Nb^{5+} , and Ta^{5+}) oxides and nitridability to form their (oxy)nitride derivatives under an NH_3 atmosphere for water splitting application

Mirabbos Hojamberdiev^a, Hajime Wagata^a, Kunio Yubuta^b, Kenta Kawashima^a, Junie Jhon M. Vequizo^c, Akira Yamakata^c, Shuji Oishi^a, Kazunari Domen^d, Katsuya Teshima^{a,e,*}

^a Department of Environmental Science and Technology, Faculty of Engineering, Shinshu University, 4-17-1 Wakasato, Nagano 380-8553, Japan

^b Institute for Materials Research, Tohoku University, 2-1-1 Katahira, Aoba-ku, Sendai 980-8577, Japan

^c Graduate School of Engineering, Toyota Technological Institute, 2-12-1 Hisakata, Tempaku, Nagoya 468-8511, Japan

^d Department of Chemical System Engineering, School of Engineering, The University of Tokyo, 7-3-1 Hongo, Bunkyo-ku, Tokyo 113-8656, Japan

^e Center for Energy and Environmental Science, Shinshu University, 4-17-1 Wakasato, Nagano 380-8553, Japan

ARTICLE INFO

Article history:

Received 24 August 2015

Received in revised form

28 September 2015

Accepted 1 October 2015

Available online 9 October 2015

Keywords:

Flux growth

Oxynitride

Visible light photocatalyst

Water splitting

Transition metal oxides

ABSTRACT

In this study, we have attempted to experimentally validate the results of previous theoretical calculations predicting the possible formation of the $\text{CdTiO}_{3-x}\text{N}_y$, CdNbO_2N , and CdTaO_2N phases by applying conventional one- and two-step fabrication methods under an NH_3 flow. For the two-step method, CdTiO_3 , $\text{Cd}_2\text{Nb}_2\text{O}_7$, and $\text{Cd}_2\text{Ta}_2\text{O}_7$ crystals were first grown by a KCl flux method, and the effects of solute concentration and cooling rate on the crystal growth were studied. The formability of their (oxy)nitride derivatives was investigated by changing the nitridation temperature (750–950 °C) and time (1–10 h) of oxide precursors. It was found that the $\text{CdTiO}_{3-x}\text{N}_y$, CdNbO_2N , and CdTaO_2N phases cannot be formed by the applied conventional methods due to the low volatilization temperature of cadmium and the susceptibility of titanium and niobium to reduction under an NH_3 atmosphere. Under high-temperature NH_3 atmosphere, only $\text{Cd}_2\text{Ta}_2\text{O}_7$ was fully converted to single-phase Ta_3N_5 . The results from the photocatalytic O_2 evolution test of bare and CoO_x -loaded Ta_3N_5 crystalline structures, converted from $\text{Cd}_2\text{Ta}_2\text{O}_7$ ($\text{Cd-Ta}_3\text{N}_5$) and Na_2CO_3 -treated Ta_2O_5 ($\text{Na-Ta}_3\text{N}_5$) and $\text{Cd}_2\text{Ta}_2\text{O}_7$ ($\text{Na-Cd-Ta}_3\text{N}_5$) crystals by nitridation at 850 °C for 20 h under an NH_3 flow, revealed that the CoO_x -loaded Ta_3N_5 showed more than two times higher O_2 evolution rate (655 μmol), whereas the CoO_x -loaded $\text{Cd-Ta}_3\text{N}_5$ and $\text{Na-Cd-Ta}_3\text{N}_5$ exhibited nearly four (501 μmol) and three (422 μmol) times higher O_2 evolution rates at 5 h compared with their bare counterparts. An improved photocatalytic activity for O_2 evolution is related to the higher density of nucleation centers of CoO_x nanoparticles in the form of dangling bonds in porous Ta_3N_5 structures and long-lived photogenerated holes, as attested by time-resolved absorption spectroscopy.

© 2015 Elsevier B.V. All rights reserved.

1. Introduction

Transition-metal oxides are a fascinating class of inorganic materials that has attracted a considerable attention due to their variety of interesting electronic, chemical and mechanical properties and technological benefits. Their electronic properties ranging

from insulating to semiconducting and conducting can be easily tailored by changing their morphologies, doping, and stoichiometry [1]. They can also be exploited for various applications at cryogenic, ambient and high temperatures because of their high Seebeck coefficients with desired thermal and electrical conductivities and heat capacities. Their abundance in nature is another important advantage for technologies to be widely adopted [2].

The partial and/or complete replacement of oxygen in transition-metal oxides with nitrogen tunes the valence states of cations, the bond covalency and the energy of the electronic states owing to its lower electronegativity, higher electronic polar-

* Corresponding author at: Center for Energy and Environmental Science, Shinshu University, 4-17-1 Wakasato, Nagano 380-8553, Japan. Fax: +81 26 269 5550.

E-mail address: teshima@shinshu-u.ac.jp (K. Teshima).

izability and higher formal anion charge relative to oxygen [3–5]. Particularly, perovskite oxynitrides of transition metals have been demonstrated as emerging materials with valuable functionalities (non-toxic pigments, colossal magnetoresistive materials, high permittivity dielectrics and photocatalysts) that contrast with that of their corresponding oxides and nitrides [6]. However, a limited number of early transition metal oxynitrides, ABO_2N ($A = \text{Ca, Sr, Ba, and La}$; $B = \text{Ti, Nb, and Ta}$), in perovskite structure have been reported to show higher photocatalytic activity in the extended visible light region for environmental remediation and energy conversion. For instance, an IPCE value of 10% at 1.2 V_{RHE} was achieved by Higashi et al. [7] using the BaTaO_2N photoanode fabricated by electrophoretic deposition (EPD) with surface modifications (co-loaded with CoO_x and RhO_x nanoparticles) at $>600 \text{ nm}$. A photoanode of particulate BaTaO_2N fabricated by a particle transfer method and modified with a Co cocatalyst surprisingly generated a photocurrent of 25 mA cm^{-2} at 1.2 V_{RHE} [8].

To achieve higher efficiency in photocatalytic water splitting, an active search for new oxynitride compounds with appropriate band gaps for visible light absorption, suitable band structures for water reduction/oxidation, and high stability under the reaction conditions is ongoing in the photocatalysis field. Recently, a number of perovskite oxynitrides, including $\text{CdTiO}_{3-x}\text{N}_y$, CdNbO_2N , and CdTaO_2N , were computationally screened to have smaller band gaps and enhanced photocatalytic activity based on the results of electronic structure calculations [9]. Also, formability of CdNbO_2N and CdTaO_2N was theoretically predicted by a calculation model utilizing the tolerance and octahedral factors [10].

In this study, we have attempted to experimentally validate the results of previous theoretical calculations predicting the possible formation of the $\text{CdTiO}_{3-x}\text{N}_y$, CdNbO_2N , and CdTaO_2N phases by applying conventional one- [11] and two-step [12,13] fabrication methods under an NH_3 atmosphere which are generally employed to produce transition-metal (oxy)nitrides. Although the crystal structures and phase transformation of perovskite-type cadmium metatitanate (CdTiO_3) [14] and pyrochlore-type cadmium pyroniobate ($\text{Cd}_2\text{Nb}_2\text{O}_7$) [15] and cadmium pyrotantalate ($\text{Cd}_2\text{Ta}_2\text{O}_7$) [16] have already been reported, this study will seek to understand the flux-induced growth of their isometric crystals and conversion to their corresponding (oxy)nitride derivatives under high-temperature NH_3 atmosphere. The effects of solute concentration and cooling rate on the flux growth of the CdTiO_3 , $\text{Cd}_2\text{Nb}_2\text{O}_7$, and $\text{Cd}_2\text{Ta}_2\text{O}_7$ crystals and the impacts of nitridation temperature and time on the formation of their corresponding (oxy)nitride derivatives under high-temperature NH_3 atmosphere were investigated. The photocatalytic water splitting activity and the behavior of photogenerated charge carriers of the Ta_3N_5 crystal structures converted from the $\text{Cd}_2\text{Ta}_2\text{O}_7$ precursor crystals by high-temperature nitridation were also demonstrated.

2. Experimental

2.1. Flux growth and high-temperature nitridation of oxide crystals

Cadmium-containing transition-metal oxide (CdTiO_3 , $\text{Cd}_2\text{Nb}_2\text{O}_7$, and $\text{Cd}_2\text{Ta}_2\text{O}_7$) crystals were grown by a flux-induced growth route, which is one of the crystal growth techniques allowing to grow crystals with high crystallinity and idiomorphic shape from a supersaturated high-temperature melt with the assistance of a flux (molten salts or metals). The stoichiometric molar quantities of TiO_2 (98.0%), Nb_2O_5 (99.9%), and Ta_2O_5 (99.9%) purchased from Wako Pure Chemical Industries Ltd. and CdO (99.0%) obtained from Strem Chemicals Inc. were manually dry mixed for 20 min with KCl (99.5%) received from Wako Pure

Chemical Industries Ltd. In this work, KCl was used as a flux for the crystal growth because of its less reactivity in this system. The solute concentration was varied from 1 to 50 mol%, the cooling rate was changed from 50 to 150°C h^{-1} , and the total mass of a solute-flux mixture was approximately 10 g for each run. After mixing, each solute-flux mixture was put into a platinum crucible and closed loosely with a platinum lid. The mixture-containing platinum crucible was then placed in a high-temperature electric muffle furnace, heated to 1000°C at a heating rate of 50°C h^{-1} , and held at this temperature for 10 h. Subsequently, the platinum crucible containing the resultant crystal product was cooled to 500°C at a cooling rate ranging 50 to 150°C h^{-1} using a cooling control program and then allowed to cool naturally to room temperature. The flux-grown oxide crystals were separated from the remaining flux by washing the resultant crystal products with hot water and dried at 100°C for 12 h. To study nitridability to form their (oxy)nitride derivatives, the CdTiO_3 , $\text{Cd}_2\text{Nb}_2\text{O}_7$, and $\text{Cd}_2\text{Ta}_2\text{O}_7$ crystals were nitrided at $750\text{--}950^\circ\text{C}$ for 1–10 h at a heating rate of $10^\circ\text{C min}^{-1}$ under an NH_3 flow (200 mL min^{-1}), as a nitriding agent, in a vertical tubular furnace. Formability of the $\text{CdTiO}_{3-x}\text{N}_y$, CdNbO_2N , and CdTaO_2N phases was additionally studied by a one-step fabrication method. The stoichiometric mixture of solute with KCl flux in a platinum crucible was heated at 950°C for 10 h at a heating rate of $10^\circ\text{C min}^{-1}$ under an NH_3 flow (200 mL min^{-1}), washed with hot water, and dried at 100°C for 12 h. The flux-grown and nitrided crystals were then subjected to crystal phase analysis and morphology observation.

2.2. Characterization

The X-ray diffraction (XRD) patterns were collected in the 2θ scan range from 5° to 80° at 30 kV and 20 mA using an X-ray diffractometer (MiniflexII, Rigaku) with $\text{Cu K}\alpha$ radiation ($\lambda = 0.15418 \text{ nm}$). The flux-grown and nitrided crystals and their surface morphologies were imaged by field-emission-type scanning electron microscopy (FE-SEM, JSM-7600F, JEOL) at an acceleration voltage of 15 kV. The crystallinity and developed facets of the flux-grown and nitrided crystals were analyzed by high-resolution transmission electron microscopy (TEM, EM-002B, TOPCON) operating at 200 kV. The ultraviolet-visible (UV–vis) diffuse reflectance spectra were obtained over a spectral range of 200–800 nm with a JASCO V-670 UV–vis-NIR spectrophotometer equipped with an integrating sphere and converted into the absorption spectra using the Kubelka–Munk function. The specific surface areas (S_{BET}) were obtained by using the Brunauer, Emmett, and Teller (BET) method from N_2 adsorption–desorption isotherms at 77 K (BELSORP-mini, BEL Japan, Inc.) on the samples degassed at 100°C for 5 h in vacuum. The chemical compositions of the flux-grown and nitrided crystals and their surface chemical compositions were thoroughly analyzed by inductively coupled plasma-optical emission spectrometry (ICP-OES, SPS5510, SII), energy-dispersive X-ray spectroscopy (EDS, JSM-7600F, JEOL), and X-ray photoelectron spectroscopy (XPS, JPS-9010MC, JEOL) using nonmonochromated $\text{Mg K}\alpha$ radiation (1253.6 eV) with a 10 mA emission current and a 10 kV acceleration voltage. The XPS profiles were fitted using a Gaussian–Lorentzian function, and the peak positions were normalized by positioning the C 1s peak at 284.5 eV.

The photocatalytic water oxidation reactions were performed in a glass vessel with 100 mg of bare or CoO_x -loaded samples in 300 mL of 10 mM AgNO_3 (99.9%, Wako Pure Chemical Industries Ltd.) aqueous solution, as an electron scavenger, under visible light irradiation (300 W Xe lamp fitted with a cold mirror (CM-1) and a cutoff filter ($\lambda > 420 \text{ nm}$)). The pH of the suspension was adjusted to 8–9 by adding 200 mg of La_2O_3 (99.9%, Wako Pure Chemical Industries Ltd.). The reaction vessel was connected to a closed-circulation system equipped with a vacuum pump and a gas chromatograph

(GC-8A, TCD, Ar carrier, Shimadzu). CoO_x (2 wt% Co) nanoparticles as a cocatalyst for water oxidation were loaded on the crystal samples by impregnating them in a $\text{Co}(\text{NO}_3)_2 \cdot 6\text{H}_2\text{O}$ (99.9%, Kanto Chemicals) aqueous solution and then heat treated under an NH_3 flow (200 mL min^{-1}) at 500°C for 1 h followed by calcination at 200°C for 1 h.

3. Results and discussion

Fig. 1 shows the XRD patterns and SEM images of CdTiO_3 (a), $\text{Cd}_2\text{Nb}_2\text{O}_7$ (b), and $\text{Cd}_2\text{Ta}_2\text{O}_7$ (c) crystals grown by a flux method using the KCl flux at 1000°C for 10 h with the cooling rate of 150°C h^{-1} and solute concentrations ranging from 1 to 50 mol%. In Fig. 1a, at 1 mol% solute concentration, Ti_6O_{11} (ICDD PDF# 50-0788), $(\text{TiO}_{1.20})_{3.12}$ (ICDD PDF# 75-0315), orthorhombic CdTiO_3 (ICDD PDF# 72-1190), and some unidentified phases were formed, due probably to the lack of cadmium supply at high temperature, as the impurity phases to the predominant rhombohedral (trigonal) CdTiO_3 phase (ilmenite) (ICDD PDF# 29-0277) with space group of $R\text{-}\bar{3}(148)$ and unit cell parameters of $a=b=5.2403 \text{ \AA}$ and $c=14.8380 \text{ \AA}$. At solute concentrations ranging from 5 to 50 mol%, the presence of the most intense (020) and (121) peaks of orthorhombic CdTiO_3 at $2\theta=23.35^\circ$ and 33.3° confirms the coexistence of the rhombohedral and orthorhombic phases of CdTiO_3 in the flux-grown crystal products. Similarly, at 1 and 5 mol% solute concentrations, some unidentified phases were formed as the impurity phases to the most prominent phases, cubic $\text{Cd}_2\text{Nb}_2\text{O}_7$ (ICDD PDF# 82-1508) with space group of $\text{Fd}\bar{3}\text{m}$ (227) and unit cell parameters of $a=b=c=10.3750 \text{ \AA}$ and cubic $\text{Cd}_2\text{Ta}_2\text{O}_7$ (ICDD PDF# 34-0405) with space group of $\text{Fd}\bar{3}\text{m}$ (227) and unit cell parameters of $a=b=c=10.3777 \text{ \AA}$, as shown in Fig. 1b and c, respectively. No diffraction peaks associated with foreign phases were noted, indicating the phase purity of the flux-grown $\text{Cd}_2\text{Nb}_2\text{O}_7$ and $\text{Cd}_2\text{Ta}_2\text{O}_7$ crystals. It can be inferred that the solute concentrations in the range of 5–50 mol% were favorable to grow single-phase rhombohedral CdTiO_3 (with a little amount of orthorhombic CdTiO_3), $\text{Cd}_2\text{Nb}_2\text{O}_7$, and $\text{Cd}_2\text{Ta}_2\text{O}_7$ crystals by a flux method using the KCl flux.

The effect of solute concentration on the morphological development of the flux-grown oxide crystals was studied by SEM, and the results are shown in Fig. 1. At 1 mol% solute concentration, CdTiO_3 crystals were observed in two different shapes: tetradecahedral and fiber. When the solute concentration was increased up to 50 mol%, the number of fibers was dramatically reduced, leaving tetradecahedral-shaped crystals to dominate. Interestingly, tetradecahedral CdTiO_3 crystals with well-developed faces and nearly the same size ($4.6 \mu\text{m}$) were grown regardless of solute concentration (Fig. 1a), implying that the growth of CdTiO_3 crystals was not completely dependent on solute concentration although more fibers were grown at low solute concentration. Furthermore, the crystal faces are thought to have similar surface energy and stability in the KCl flux with different solute concentrations, resulting in the growth of tetradecahedral crystals, and the twinned crystals were not observed. Compared with the CdTiO_3 crystals, the influence of solute concentration on the morphologies of $\text{Cd}_2\text{Nb}_2\text{O}_7$ and $\text{Cd}_2\text{Ta}_2\text{O}_7$ crystals can easily be seen in Fig. 1b and c. That is, at 1 mol% solute concentration, $\text{Cd}_2\text{Nb}_2\text{O}_7$ crystals possessed irregular shape and size, whereas an increase in solute concentration up to 10 mol% facilitated to gain their nearly identical octahedral shape and size. However, the well-developed octahedral shape of some crystals started loosening with further increase to 20 mol% and nearly disappeared at 50 mol%, while somehow maintained their average crystal size of $18.5 \mu\text{m}$. In Fig. 1c, a profound effect of solute concentration on the morphology of $\text{Cd}_2\text{Ta}_2\text{O}_7$ crystals can be markedly noted. Specifically, the crystals gained their octahedral

shape with well-developed faces when the solute concentration was set to 1 mol%. An increase in solute concentration to 5 and 10 mol% led to the formation of $\text{Cd}_2\text{Ta}_2\text{O}_7$ crystals with a truncated octahedral shape without altering the average crystal size of $4.2 \mu\text{m}$. In addition to the truncated octahedral large crystals, the solute concentrations of 20 and 50 mol% gave rise to the growth of irregular submicron crystals with average size of 137 nm due to the presence of a large number of nuclei, hindering the complete growth of crystals even the high-temperature solution became critically supersaturated [13]. Compared to the CdTiO_3 crystals, the loss of crystal habits in the $\text{Cd}_2\text{Nb}_2\text{O}_7$ and $\text{Cd}_2\text{Ta}_2\text{O}_7$ crystals grown at high solute concentrations is indicative of the low solubility of solute (i.e., semi-solid state reaction) because of insufficient amount of KCl flux [17]. This certainly evidences an important role of the flux amount in reaching the equilibrium and crystal growth. Generally speaking, the use of KCl flux seemingly reduced the difference in surface energies between the faces (or blocking the growth of other faces), resulting in the growth of specific octahedral $\text{Cd}_2\text{Nb}_2\text{O}_7$ crystals with well-defined $\{111\}$ faces. In contrast, the $\{111\}$ and $\{100\}$ faces appeared to be stable, allowing the $\text{Cd}_2\text{Ta}_2\text{O}_7$ crystals to gain their truncated octahedral shapes. Although several factors are simultaneously responsible for the final shapes of the flux-grown crystals, the crystal habit is believed to be originated from the different energies of interfaces between the flux compensating the strength of dangling bonds through the secondary interactions and crystal surface, depending on the flux type used and crystallographic orientation of the facets [18]. To thoroughly interpret the entire growth mechanisms for these crystals, more systematic studies need to be performed.

To study the effect of cooling rate on the growth of CdTiO_3 , $\text{Cd}_2\text{Nb}_2\text{O}_7$, and $\text{Cd}_2\text{Ta}_2\text{O}_7$ crystals, the resultant crystal products were cooled at cooling rates in the brief range of $50\text{--}150^\circ\text{C h}^{-1}$. The XRD patterns and SEM images of the crystal products grown with cooling rates of 50, 100, and 150°C h^{-1} are compiled in Fig. 2. The XRD results revealed that the phase-pure crystals can be grown in this brief range of cooling rate. It should also be mentioned that the formation of orthorhombic CdTiO_3 as an impurity phase to rhombohedral CdTiO_3 was unavoidable at this range of cooling rate. Compared with the CdTiO_3 crystals (Fig. 2a), the cooling rate slightly affected the morphology of $\text{Cd}_2\text{Nb}_2\text{O}_7$ and $\text{Cd}_2\text{Ta}_2\text{O}_7$ crystals. Namely, the size of octahedral $\text{Cd}_2\text{Nb}_2\text{O}_7$ crystals became comparatively smaller with increasing the cooling rate (Fig. 2b), suggesting that a slower cooling rate facilitated the growth of crystals. At cooling rates of 50 and 100°C h^{-1} , the propagation of crystal facets by the attachment of growth units onto step edges was incomplete in the truncated octahedral $\text{Cd}_2\text{Ta}_2\text{O}_7$ crystals in spite of the growth of larger crystals, and terrace, steps, and even “island” crystals can be clearly seen in Fig. 2c. The formation of “islands” with identical crystal habit on the surfaces of parent single crystals was likely caused by the strong adatom–adatom interactions rather than the adatom with the surface (Volmer–Weber growth) [19]. At a slightly faster cooling rate (150°C h^{-1}), the thermal fluctuations of steps were assumed to be sufficiently rapid to produce an abundance of kink sites for the attachment of growth units, completing the growth of the well-defined facets of crystals with smaller size. As these crystals were grown in the KCl flux that may also act as an impurity, an impurity-step interaction can also be taken into account as one of the possible mechanisms determined by the kinetics of the attachment and detachment of growth units [20], which rather differs from the classical Burton–Cabrera–Frank (BCF) model [21]. Here we conclude that under the current experimental conditions, the growth processes of CdTiO_3 and $\text{Cd}_2\text{Nb}_2\text{O}_7$ crystals are less perceptive to the cooling rate than that of the $\text{Cd}_2\text{Ta}_2\text{O}_7$ crystals.

As an important part of this study, the thermal conversion of the flux-grown perovskite-type CdTiO_3 and pyrochlore-

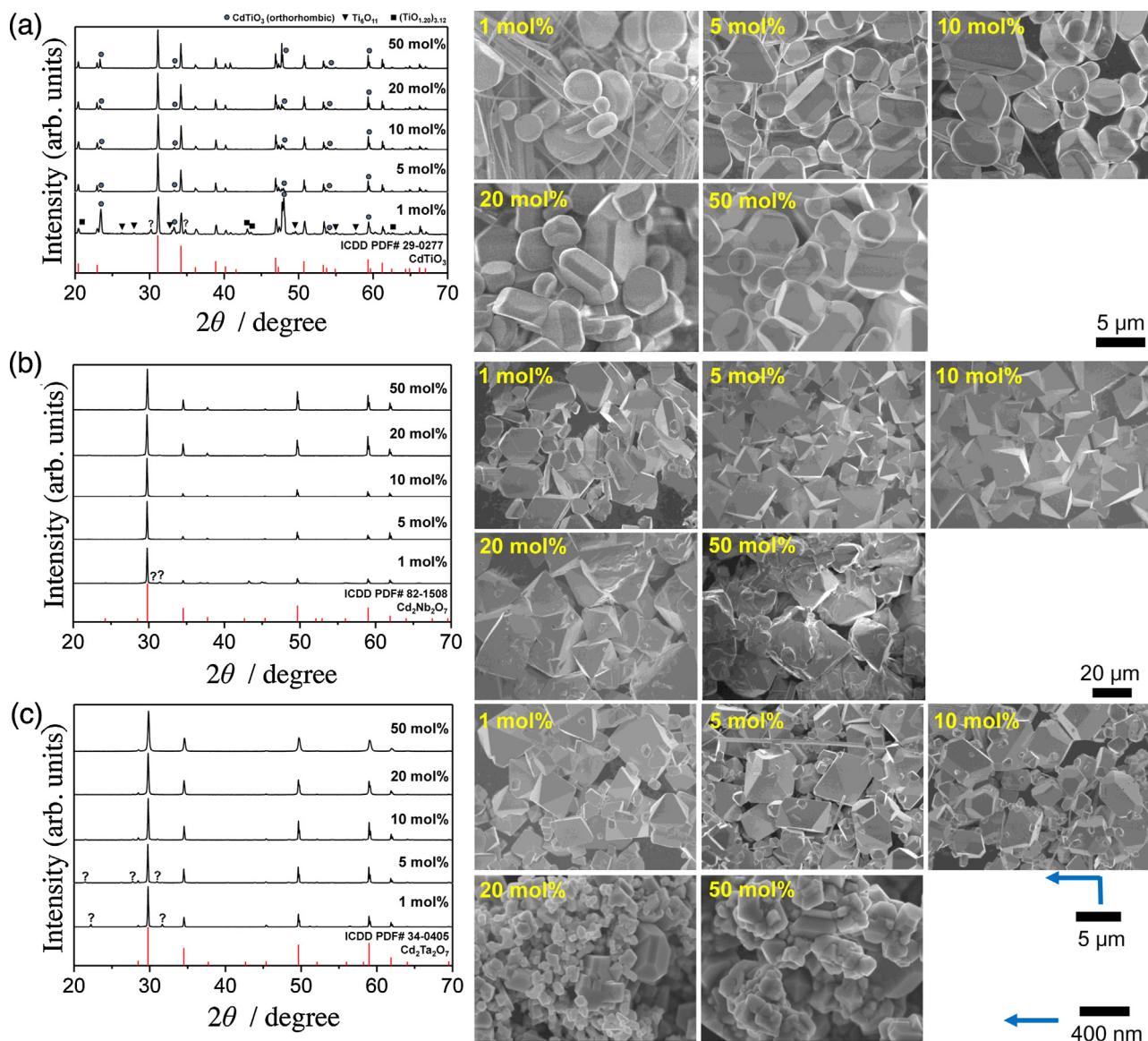


Fig. 1. XRD patterns and SEM images of (a) CdTiO_3 , (b) $\text{Cd}_2\text{Nb}_2\text{O}_7$, and (c) $\text{Cd}_2\text{Ta}_2\text{O}_7$ crystals grown by a KCl flux method at 1000°C for 10 h with solute concentrations of 1–50 mol% and cooling rate of 150°C h^{-1} .

type $\text{Cd}_2\text{Nb}_2\text{O}_7$ and $\text{Cd}_2\text{Ta}_2\text{O}_7$ crystals to their corresponding (oxy)nitride derivatives was studied by applying conventional one- and two-step fabrication methods under an NH_3 flow at 750 – 950°C for 1–10 h that have been routinely used to fabricate transition-metal (oxy)nitrides. The XRD patterns and SEM images of the nitrided samples are summarized in Figs. 3 and 4 with respect to their oxide precursors. As shown in Fig. 3a, by nitriding the crystal samples at 750 – 950°C for 1–10 h, CdTiO_3 was completely converted to TiN (ICDD PDF# 74-8388) through the CdTiO_3 (including orthorhombic CdTiO_3) \rightarrow rutile- TiO_2 (ICDD PDF# 21-1276) + TiO (ICDD PDF# 71-5272) \rightarrow TiO (ICDD PDF# 08-0117) transition process, while $\text{Cd}_2\text{Nb}_2\text{O}_7$ underwent the following phase transitions: $\text{Cd}_2\text{Nb}_2\text{O}_7 \rightarrow \text{Nb}_{3.49}\text{Nb}_{4.56}\text{O}_{0.44}$ (ICDD PDF# 89-1202) + NbON (ICDD PDF# 50-1175) + unidentified phases $\rightarrow \text{Nb}_{3.49}\text{Nb}_{4.56}\text{O}_{0.44} \rightarrow \text{NbN}_{0.801}$ (ICDD PDF# 74-0780) \rightarrow NbN (ICDD PDF# 73-2895) + Nb_2N (ICDD PDF# 50-0802) + unidentified phases $\rightarrow \text{Nb}_{0.987}\text{N}$ (ICDD PDF# 89-2908) + Nb_2N + unidentified phases in the same nitridation temperature range (Fig. 3b). Compared with CdTiO_3 and $\text{Cd}_2\text{Nb}_2\text{O}_7$, the $\text{Cd}_2\text{Ta}_2\text{O}_7$ was simply converted to TaON (ICDD

PDF# 70-1193) \rightarrow TaON + monoclinic- Ta_3N_5 (ICDD PDF# 89-5200) \rightarrow orthorhombic- Ta_3N_5 (ICDD PDF# 79-1533) (Fig. 3c). Unexpectedly, the nitridation of CdTiO_3 , $\text{Cd}_2\text{Nb}_2\text{O}_7$, and $\text{Cd}_2\text{Ta}_2\text{O}_7$ proceeded in a different way because of low volatilization temperature of cadmium and high susceptibility of titanium and niobium to reduction under high-temperature NH_3 atmosphere, leading to the formation of various transition metal (oxy)nitrides, depending on nitridation temperature and time. It can be concluded that within the nitridation temperatures and times applied in this study, no formation of the $\text{CdTiO}_{3-x}\text{N}_y$, CdNbO_2N , and CdTaO_2N phases was observed by applying conventional one- and two-step fabrication methods under an NH_3 flow. Furthermore, as the perovskite-type oxide precursor, CdTiO_3 contains a B-site cation with the highest oxidation state of +4 (as further oxidation of Ti^{4+} is not possible, and the reduction of Ti^{4+} to Ti^{3+} is expected under high-temperature NH_3 atmosphere), which could not fully compensate the increasing negative charges resulted from nitrogen incorporation in the anionic substructure [22]. In contrast, the pyrochlore-type oxide precursors ($\text{Cd}_2\text{Nb}_2\text{O}_7$ and $\text{Cd}_2\text{Ta}_2\text{O}_7$), in which the oxidation states of A- and B-site cations are assumed

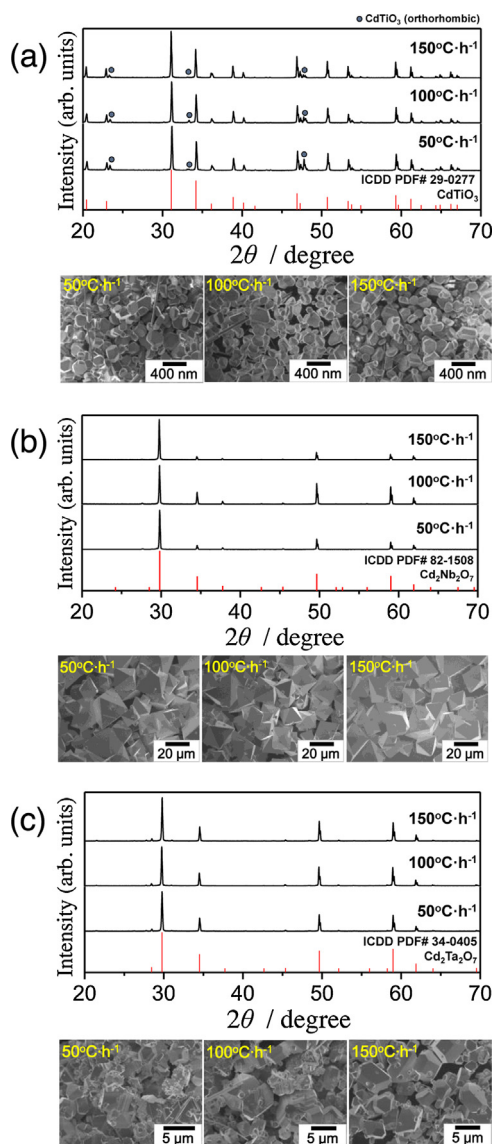


Fig. 2. XRD patterns and SEM images of (a) CdTiO₃, (b) Cd₂Nb₂O₇, and (c) Cd₂Ta₂O₇ crystals grown by a KCl flux method at 1000 °C for 10 h with solute concentration of 10 mol% and cooling rates of 50–150 °C h⁻¹.

not to change significantly upon thermal conversion to perovskite oxynitride, were expected to form CdNbO₂N and CdTaO₂N.

In addition to the two-step fabrication method, we also employed a one-step fabrication method using the KCl flux. Interestingly, similar results were obtained, as shown in Fig. A.1 (Supplementary material). Although their feasible formability was predicted based on the calculated tolerance ($t = 0.935711$) and octahedral ($r_B/r_X = 0.44674963$) factors [10], these phases however could not form due to the volatilization of cadmium under NH₃ atmosphere and structural rearrangement.

It seems that the tolerance and octahedral factors are necessary but additional factors should also be considered to provide sufficient conditions for the complete formation of some perovskite oxynitrides predicted. Interestingly, the nitrated samples retained the original shapes of isotropic oxide crystals regardless of nitridation temperature and time, as shown in Fig. 3, confirming that the applied heating and cooling rates were favorable to maintain the crystal outline. Fig. 4 shows the overview and surface texture of the crystal samples before and after nitridation and evidences that the crystal samples after high-temperature

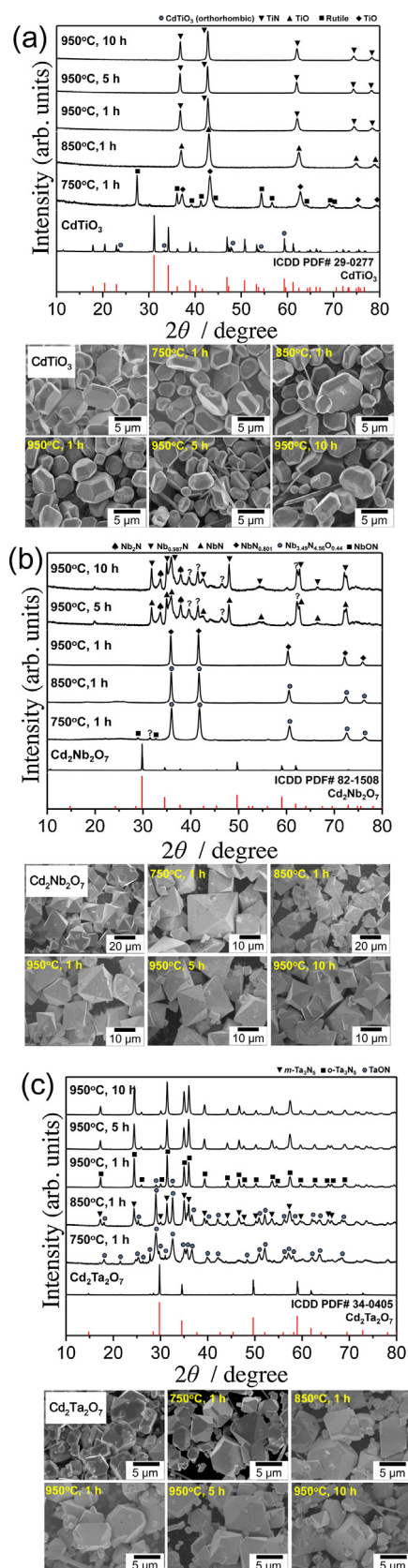


Fig. 3. XRD patterns and SEM images of (a) CdTiO₃, (b) Cd₂Nb₂O₇, and (c) Cd₂Ta₂O₇ crystals after nitridation at 750–950 °C for 1–10 h under an NH₃ flow.

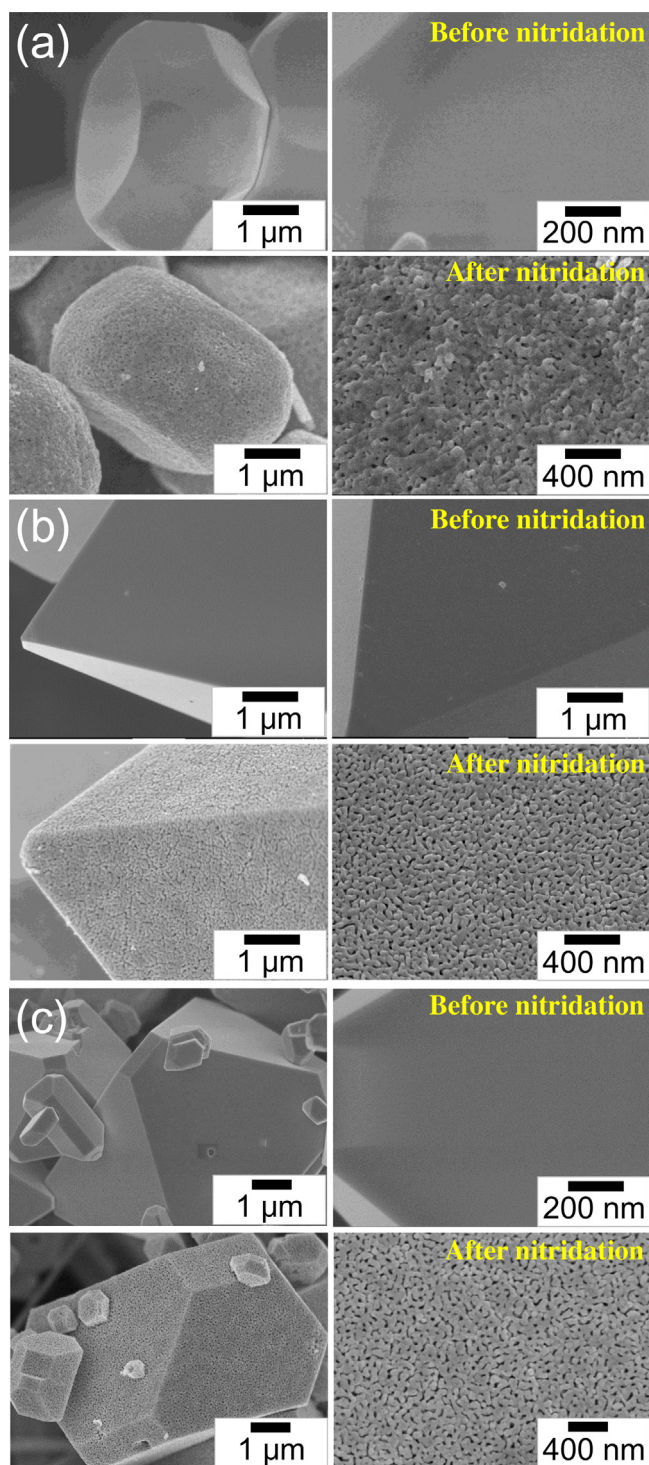


Fig. 4. Overview (left) and surface texture (right) of (a) CdTiO_3 , (b) $\text{Cd}_2\text{Nb}_2\text{O}_7$, and (c) $\text{Cd}_2\text{Ta}_2\text{O}_7$ crystals grown by a KCl flux method with solute concentration of 10 mol% before and after nitridation at 950°C for 10 h under an NH_3 flow.

nitridation possess highly porous structures emerged from the strong segregation of nanocrystals. These highly porous structures were formed possibly through the lattice condensation process caused by the replacement of O^{2-} with N^{3-} in the anionic network and the volatilization of cadmium [13,23–25]. The surface textures of the samples obtained by nitridation of the $\text{Cd}_2\text{Nb}_2\text{O}_7$ and $\text{Cd}_2\text{Ta}_2\text{O}_7$ crystals are nearly identical compared to that of the sample obtained by nitriding the CdTiO_3 crystals. Probably, this dif-

ference arises from the difference in lattice condensation process and structural rearrangement.

Due to the volatilization of cadmium and susceptibility of titanium and niobium to the reduction under high-temperature NH_3 atmosphere, only $\text{Cd}_2\text{Ta}_2\text{O}_7$ was completely converted to single-phase Ta_3N_5 , which is also a visible-light-responsive photocatalyst. Therefore, the crystallographic characteristics of the flux-grown $\text{Cd}_2\text{Ta}_2\text{O}_7$ and as-converted Ta_3N_5 crystals were examined by TEM, and the results are illustrated in Fig. 5. The bright-field TEM images in Fig. 5a and c confirm that the flux-grown $\text{Cd}_2\text{Ta}_2\text{O}_7$ crystals are in the form of truncated octahedron, whereas Fig. 5b and d reveal that porous Ta_3N_5 crystalline structures converted from the $\text{Cd}_2\text{Ta}_2\text{O}_7$ precursor crystals by nitridation under an NH_3 flow are composed of joined nanocrystals of Ta_3N_5 . Thus, the Ta_3N_5 crystalline structures consist of nanoligament, and as a result, the selected-area electron diffraction (SAED) pattern of the Ta_3N_5 crystalline structures (inset of Fig. 5b) exhibits the Debye–Scherrer rings, characteristic of polycrystallinity. The lattice images of the $\text{Cd}_2\text{Ta}_2\text{O}_7$ crystals and Ta_3N_5 crystalline structures, shown in Fig. 5e and f, were taken with incident beam along the $[5\bar{1}0]$ and $[010]$ directions, respectively. No clear defects were observed in these lattice images, confirming the high crystallinity of the $\text{Cd}_2\text{Ta}_2\text{O}_7$ crystals and Ta_3N_5 crystalline structures. The size of the Ta_3N_5 crystallites was too small to obtain a conventional SAED pattern, and nano-beam electron diffraction (NBED) was therefore applied for a small area, resulting in disc-like diffraction spots instead of small dots. The TEM observation results confirmed that each of these segregated nanocrystals of Ta_3N_5 has a single crystalline nature and is randomly orientated. In Fig. 5g and h, periodically highly ordered diffraction spots in the SAED and NBED patterns of the flux-grown $\text{Cd}_2\text{Ta}_2\text{O}_7$ and as-converted Ta_3N_5 crystallites indicate their single-crystalline nature, respectively. In the NBED pattern of the Ta_3N_5 crystallites (Fig. 5h), the d_{002} and d_{200} spacings were determined to be 0.5116 nm which is in good agreement with the theoretical values of the d_{002} and d_{200} planes (0.5115 nm). Indexing of the SAED pattern of the flux-grown $\text{Cd}_2\text{Ta}_2\text{O}_7$ crystal (Fig. 5g) confirms the presence of a typical cubic lattice structure without notable defects. The diffraction spots that originated from the $\{111\}$ and $\{100\}$ faces can be indexed. As shown in the SEM image (Fig. 5j), the dominant equilateral-triangle-shaped faces in the octahedral crystals of $\text{Cd}_2\text{Ta}_2\text{O}_7$ are $\{111\}$ and rectangle-shaped faces are $\{100\}$. The face angle of $\theta_{(111)\wedge(100)}$ in the cubic system with $\text{Fd}\bar{3}\text{m}$ space group is 54.736° , which corresponds to that of the flux-grown $\text{Cd}_2\text{Ta}_2\text{O}_7$ crystal ($\theta_{(111)\wedge(100)} = 55^\circ$). In Fig. 5i, the simulated shape of a crystal dominantly surrounded with $\{111\}$ faces and less dominantly surrounded with $\{100\}$ faces belonging to the cubic system with $\text{Fd}\bar{3}\text{m}$ space group corresponds with the shape of the flux-grown $\text{Cd}_2\text{Ta}_2\text{O}_7$ crystals shown in the SEM image (Fig. 5j).

Fig. 6 shows the UV–vis diffuse reflectance spectra of the as-grown $\text{Cd}_2\text{Ta}_2\text{O}_7$ crystals and nitrided samples at 750 – 950°C for 1–10 h under an NH_3 flow. The $\text{Cd}_2\text{Ta}_2\text{O}_7$ crystals show an absorption edge of 400 nm, corresponding to a band gap energy of approximately 3.10 eV, signifying its photocatalytic activity under UV light. In contrast, the absorption edge was shifted to higher wavelength for the nitrided samples. That is, the absorption edges exhibited by the nitrided samples were found to be approximately 600 nm, corresponding to a band gap energy of approximately 2.06 eV, which is consistent with the previously reported data [26].

The shift in absorption edge from 400 to 600 nm was caused by the simultaneous formation of mixed phases of TaON and Ta_3N_5 because of the volatilization of cadmium under high-temperature NH_3 atmosphere and the complete conversion of the mixed phases of TaON and Ta_3N_5 to single-phase Ta_3N_5 (Fig. 3c). The complete substitution of nitrogen for oxygen resulted in the higher negative potential of the valence band and the narrowing of the band gap compared to that of TaON because N 2p orbitals have higher

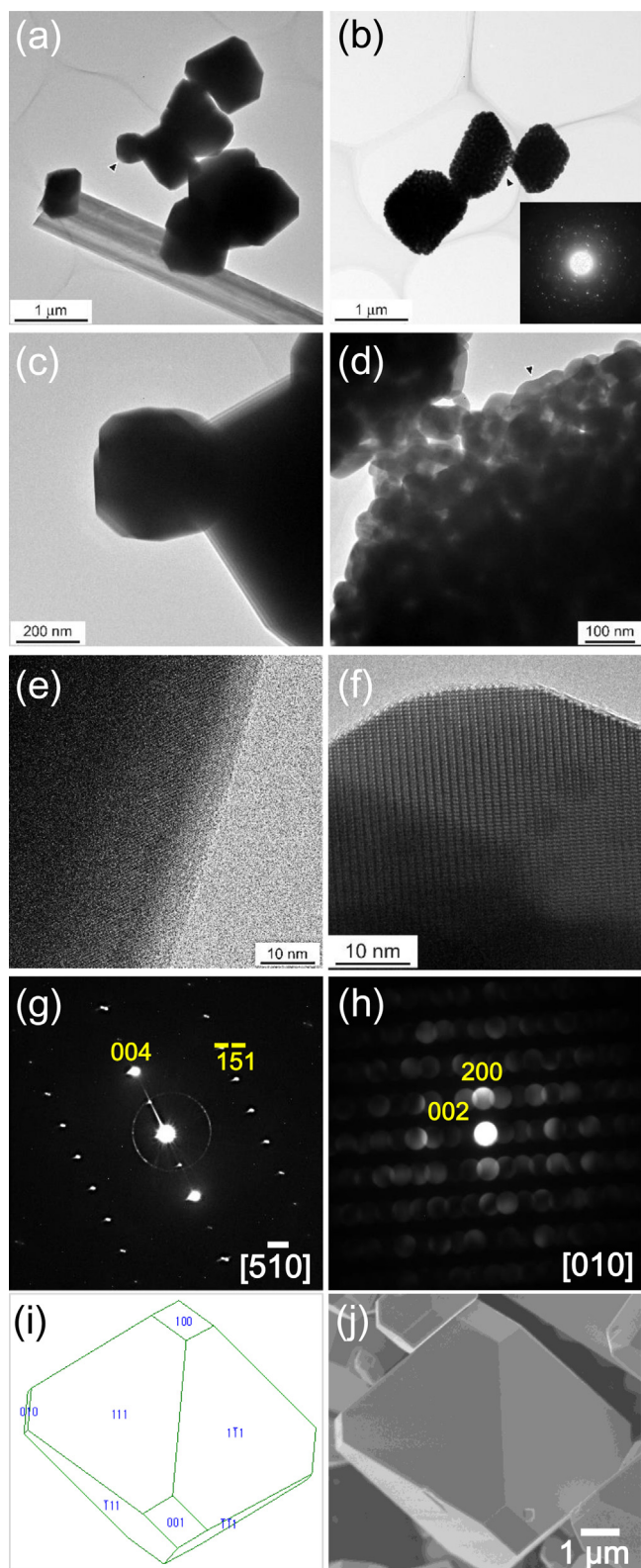


Fig. 5. TEM and HRTEM images and SAED patterns of (a,c,e,g) $\text{Cd}_2\text{Ta}_2\text{O}_7$ crystals grown by a KCl flux method at 1000°C for 10 h with solute concentration of 10 mol% and (b,d,f,h) Ta_3N_5 crystalline structures converted from $\text{Cd}_2\text{Ta}_2\text{O}_7$ crystals by nitridation at 950°C for 10 h under an NH_3 flow. (i) An illustrative sketch and (j) SEM image of $\text{Cd}_2\text{Ta}_2\text{O}_7$ crystal surrounded by the $\{111\}$ and $\{110\}$ faces.

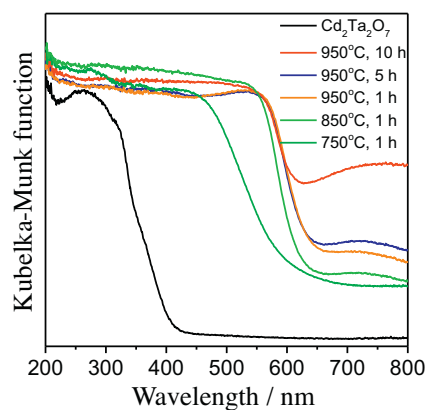


Fig. 6. UV-vis diffuse reflectance spectra of $\text{Cd}_2\text{Ta}_2\text{O}_7$ crystals grown by a KCl flux method at 1000°C for 10 h with solute concentration of 10 mol% before and after nitridation at 750 – 950°C for 1–10 h under an NH_3 flow.

potential energies than O 2p [27,28]. For the nitrated samples, the slope of the UV-vis spectra became steeper with increasing the nitridation temperature and time due to the gradual conversion of the mixed phases of TaON and Ta_3N_5 to single-phase Ta_3N_5 . Meantime, the intensity of the background absorption beyond the absorption edge increased with increasing the nitridation temperature and time, which is generally indicative of the presence of increased defects associated with the reduced tantalum species and anion deficiency [29,30]. It can be deduced that highly porous Ta_3N_5 crystalline structures with their retained isometric shapes and high crystallinity are expected to show better photocatalytic activity for water splitting and the decomposition of organic pollutants under visible light irradiation.

The chemical composition was analyzed by EDS, XPS, and ICP to trace the amounts of cadmium, potassium, and nitrogen as well as the oxidation state of tantalum in the flux-grown $\text{Cd}_2\text{Ta}_2\text{O}_7$ crystals and as-converted Ta_3N_5 crystalline structures, and the results are compiled in Fig. 7. First, to confirm the elemental distribution, EDS was conducted on the Ta_3N_5 crystalline structures. In Fig. 7a–c, the EDS mapping images reveal that Ta and N elements are homogeneously distributed within the isotropic Ta_3N_5 crystalline structures. The corresponding EDS spectrum and XPS survey scan in Fig. 7d and e imply that only Ta and N elements with a stoichiometric Ta_3N_5 composition are present on the surfaces of crystalline structures, and the signals of residual carbon and oxygen arisen from adventitious contamination are also observed. However, the signals attesting the presence of cadmium and potassium were not detected. Further to that, additional ICP analysis was performed to estimate the exact amounts of impurities: potassium from the KCl flux and remaining cadmium from the $\text{Cd}_2\text{Ta}_2\text{O}_7$ precursor. As shown in the inset of Fig. 7e, a negligible amount of potassium was unintentionally incorporated into the Ta_3N_5 crystalline structures, while cadmium was completely volatilized during high-temperature nitridation of $\text{Cd}_2\text{Ta}_2\text{O}_7$ crystals under an NH_3 flow.

The Ta 4f, Cd 3d, O 1s, and N 1s core-level spectra of the flux-grown $\text{Cd}_2\text{Ta}_2\text{O}_7$ crystals and as-converted Ta_3N_5 crystal structures are shown in Fig. 7f. In $\text{Cd}_2\text{Ta}_2\text{O}_7$, the Cd 3d peaks centered at 404.5 and 411.3 eV are originated from the Cd 3d_{5/2} and Cd 3d_{3/2} spin-orbit splitting, and the Ta 4f peaks appeared at 25.5 and 27.4 eV correspond to the Ta 4f_{7/2} and Ta 4f_{5/2} spin-orbit splitting. Both doublets show narrow symmetrical lines, confirming unique chemical states for Cd and Ta in the $\text{Cd}_2\text{Ta}_2\text{O}_7$. The energy position of the Ta 4f peaks in $\text{Cd}_2\text{Ta}_2\text{O}_7$ is close to the binding energy of Ta in $\text{Sr}_2\text{Ta}_2\text{O}_7$ [31]. As expected, the Ta 4f peaks for the Ta_3N_5 were shifted to lower binding energies by ca. 1.58 eV compared to that of $\text{Cd}_2\text{Ta}_2\text{O}_7$. Considering the difference in electronegativity between O and N, it

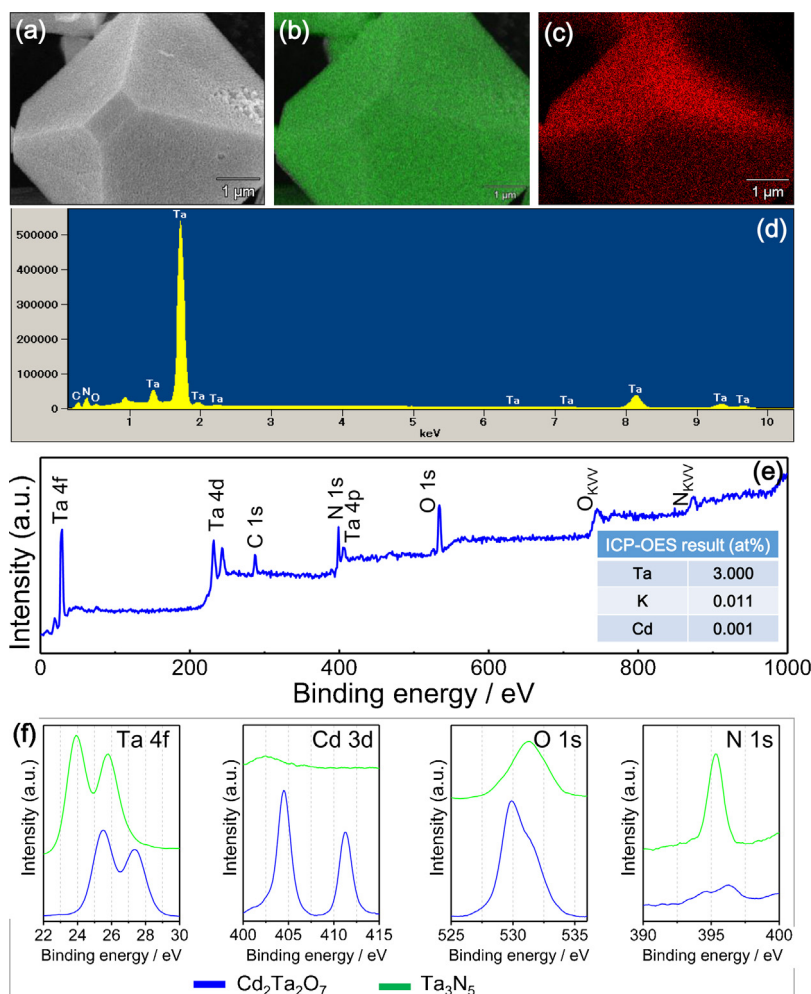


Fig. 7. EDS analyses: (a) grey image, (b) Ta mapping image, (c) N mapping image, and (d) corresponding spectrum, (e) wide-scan XPS spectrum, and (inset) ICP data of Ta_3N_5 crystalline structures converted from $\text{Cd}_2\text{Ta}_2\text{O}_7$ crystals by nitridation at 950°C for 10 h under an NH_3 flow. (f) Ta 4f, Cd 3d, O 1s, and N 1s core-level spectra of the $\text{Cd}_2\text{Ta}_2\text{O}_7$ crystals (blue) and Ta_3N_5 crystal structures (green). (For interpretation of the references to color in this figure legend, the reader is referred to the web version of this article.)

is believed that the electron density around the Ta atom increased drastically with the complete replacement of oxygen with nitrogen, affecting the band gap positions of the $\text{Cd}_2\text{Ta}_2\text{O}_7$ and Ta_3N_5 [32]. The peak centered at 395.3 eV is assigned to the Ti–N bond. The O 1s spectrum was fitted with two Gaussian components: the main peak at 529.8 eV is assigned to the Ta–O bond, and a small one at 531.6 eV is generally associated with the surface oxygen contamination [33].

The time courses of the photocatalytic O_2 evolution over bare and CoO_x -loaded Ta_3N_5 crystalline structures, converted from $\text{Cd}_2\text{Ta}_2\text{O}_7$ ($\text{Cd-Ta}_3\text{N}_5$) and Na_2CO_3 -treated Ta_2O_5 ($\text{Na-Ta}_3\text{N}_5$) and $\text{Cd}_2\text{Ta}_2\text{O}_7$ ($\text{Na-Cd-Ta}_3\text{N}_5$) crystals by nitridation at 850°C for 20 h under an NH_3 flow, under visible light irradiation ($\lambda > 420\text{ nm}$) are shown in Fig. 8. Note that the photocatalytic water oxidation experiments with $\text{Na-Ta}_3\text{N}_5$ and $\text{Na-Cd-Ta}_3\text{N}_5$ were conducted only for comparison. The detailed fabrication process [34] and characterization results of the $\text{Na-Ta}_3\text{N}_5$ and $\text{Na-Cd-Ta}_3\text{N}_5$ samples are shown in Figs. A.2 and A.3 (Supplementary material). No water oxidation half-reaction proceeded in the dark. Upon visible light irradiation, a negligible amount of N_2 gas ($\sim 2.32\text{ }\mu\text{mol}$) was evolved in the initial stage of the reaction due to the oxidation of N^{3-} species near the surface of Ta_3N_5 crystals. In the case of bare samples, the rate of O_2 evolution was two times higher in the $\text{Na-Ta}_3\text{N}_5$ ($296\text{ }\mu\text{mol}$) compared to that of the $\text{Cd-Ta}_3\text{N}_5$ and $\text{Na-Cd-Ta}_3\text{N}_5$ samples ($137\text{ }\mu\text{mol}$) at 5 h. Despite a slightly higher rate of O_2 evolution over the $\text{Na-Cd-Ta}_3\text{N}_5$ in the initial stage, the O_2 evolution

rates for the $\text{Cd-Ta}_3\text{N}_5$ and $\text{Na-Cd-Ta}_3\text{N}_5$ became nearly the same at 5 h, and the Na_2CO_3 -treatment did not significantly improve the O_2 evolution rate, as observed in the previous study [34]. Compared with their bare analogues, CoO_x (2 wt% Co) cocatalyst-loaded $\text{Na-Ta}_3\text{N}_5$ showed more than two times higher O_2 evolution rate ($655\text{ }\mu\text{mol}$), whereas the CoO_x -loaded $\text{Cd-Ta}_3\text{N}_5$ and $\text{Na-Cd-Ta}_3\text{N}_5$ exhibited nearly four ($501\text{ }\mu\text{mol}$) and three ($422\text{ }\mu\text{mol}$) times higher O_2 evolution rates at 5 h.

Compared with $\text{Cd-Ta}_3\text{N}_5$ and $\text{Na-Cd-Ta}_3\text{N}_5$, higher O_2 evolution rate of $\text{Na-Ta}_3\text{N}_5$ is related to its smaller particle size (125 nm for $\text{Na-Ta}_3\text{N}_5$, $4.3\text{ }\mu\text{m}$ for $\text{Cd-Ta}_3\text{N}_5$, and $4.2\text{ }\mu\text{m}$ for $\text{Na-Cd-Ta}_3\text{N}_5$), higher specific surface area ($16.4\text{ m}^2\text{ g}^{-1}$ for $\text{Na-Ta}_3\text{N}_5$, $5.2\text{ m}^2\text{ g}^{-1}$ for $\text{Cd-Ta}_3\text{N}_5$, and $4.9\text{ m}^2\text{ g}^{-1}$ for $\text{Na-Cd-Ta}_3\text{N}_5$), higher crystallinity, lower defect density, less grain boundaries, and better dispersion of CoO_x nanoparticles [35,36]. Smaller particle size of the $\text{Na-Ta}_3\text{N}_5$ was expected to reduce the migration distance of photogenerated charge carriers to the surface active sites [37], leading to higher O_2 evolution rate, while a marginally contradicting event took place in the $\text{Cd-Ta}_3\text{N}_5$ and $\text{Na-Cd-Ta}_3\text{N}_5$ with larger particle size and increased dimension [38]. Moreover, a great number of grain boundaries were formed due to the segregation of nanocrystals and reduced tantalum species and anionic vacancies (deep donor states) because of prolonged nitridation time have additionally caused the lower O_2 evolution rates in the $\text{Cd-Ta}_3\text{N}_5$ and $\text{Na-Cd-Ta}_3\text{N}_5$ [39–41]. Compared with CoO_x -

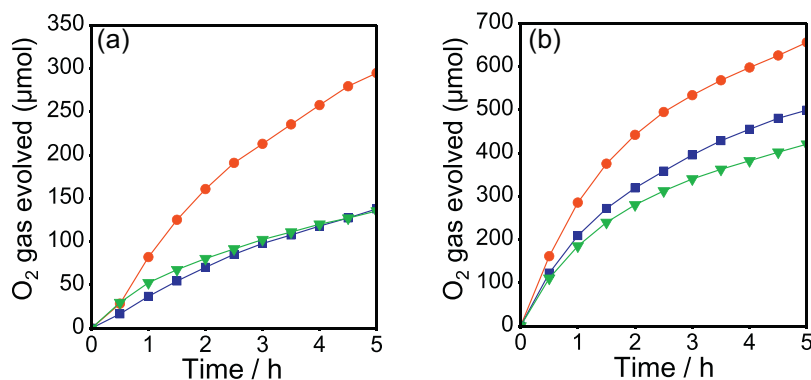


Fig. 8. Time courses of photocatalytic O₂ evolution over (a) bare and (b) CoO_x-loaded Ta₃N₅ crystalline structures converted from Cd₂Ta₂O₇ (Cd-Ta₃N₅, square) and Na₂CO₃-treated Ta₂O₅ (Na-Ta₃N₅, circle) and Cd₂Ta₂O₇ (Na-Cd-Ta₃N₅, triangle) crystals by nitridation at 850 °C for 20 h under an NH₃ flow.

loaded Na-Ta₃N₅, a drastic increase in the O₂ evolution rates of Cd-Ta₃N₅ and Na-Cd-Ta₃N₅ by loading CoO_x cocatalyst is presumably associated with the dispersion of CoO_x nanoparticles. Porous crystalline structures are thought to have more dangling bonds [42] compared with CoO_x-loaded Na-Ta₃N₅ with smooth surfaces, and therefore, the density of nucleation centers in the form of dangling bonds was higher in Cd-Ta₃N₅ and Na-Cd-Ta₃N₅, resulting much higher O₂ evolution rates (Fig. A.4 (Supplementary material)). As reported previously, a complete volatilization of Ge (1–5%) from the Ta₃N₅ photoanodes could improve the photocurrent because the volatilization of Ge reduced the amount of N vacancies in the Ta₃N₅ lattice by acting as a fluxing agent [43]. Since Cd was totally volatilized at low nitridation temperature under an NH₃ flow, its contribution as a fluxing agent to the reduction of nitrogen vacancies in Cd-Ta₃N₅ and Na-Cd-Ta₃N₅ at high nitridation temperature cannot be taken into account in this study (Fig. 8).

To gain a deeper insight into the contribution of defect density on the O₂ evolution rate, bare samples were analyzed by time-resolved absorption (TA) spectroscopy [44], and the results are shown Fig. 9. As shown, the TA spectra of bare Na-Ta₃N₅, Cd-Ta₃N₅, and Na-Cd-Ta₃N₅ samples show absorption peaks at 17000 cm⁻¹, which are ascribed to the photogenerated holes. The absorption intensity at 17000 cm⁻¹ of Na-Ta₃N₅ is much higher than that of Cd-Ta₃N₅ and Na-Cd-Ta₃N₅, suggesting that the number of surviving holes in Na-Ta₃N₅ is much greater than that in Cd-Ta₃N₅ and Na-Cd-Ta₃N₅. In terms of the number of surviving holes, the samples can be placed in the following order: Na-Ta₃N₅ >> Na-Cd-Ta₃N₅ > Cd-Ta₃N₅. The broad absorption at 14000–4000 cm⁻¹ can be assigned to the transient absorption of deeply trapped electrons and/or holes at the defects. This absorption intensity is higher in Na-Ta₃N₅ than in Cd-Ta₃N₅ and Na-Cd-Ta₃N₅, indicating that electron and/or hole are deeply trapped at defects in Na-Ta₃N₅ [45,46]. The absorption below 4000 cm⁻¹ is associated with shallowly trapped electrons and/or free electrons. Note that the apparent decrease of absorption below 3000 cm⁻¹ is due to heat or emission, giving a negative signal below 2200 cm⁻¹. The absorption in the mid-IR region for Na-Ta₃N₅ decreases towards lower wavenumber, whereas for Cd-Ta₃N₅ and Na-Cd-Ta₃N₅, the absorption shows totally different behavior, namely, increasing towards lower wavenumber, as shown in the insets of Fig. 9. These results suggest that the number of free and/or shallowly trapped electrons in Cd-Ta₃N₅ and Na-Cd-Ta₃N₅ is higher than that in Na-Ta₃N₅. Because of higher number of surviving holes, Na-Ta₃N₅ showed higher photocatalytic activity for water oxidation compared to both Cd-Ta₃N₅ and Na-Cd-Ta₃N₅. As shown in Fig. A.5 (Supplementary material), the lifetimes of photogenerated charge carriers on samples with different defect densities are longer than milliseconds, evidencing the decisive con-

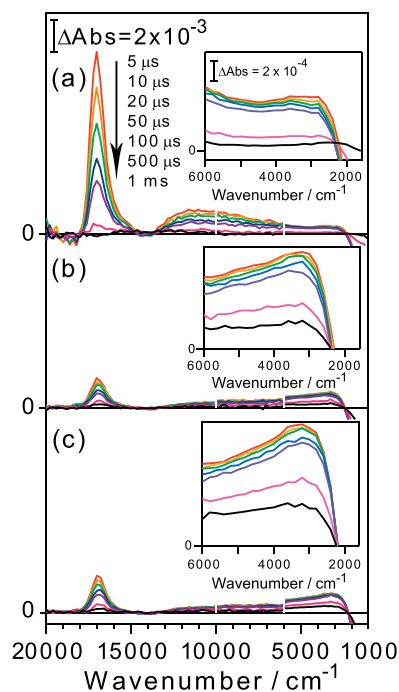


Fig. 9. Transient absorption spectra of bare Ta₃N₅ crystalline structures converted from Na₂CO₃-treated Ta₂O₅ (Na-Ta₃N₅, a), Cd₂Ta₂O₇ (Cd-Ta₃N₅, b), and Na₂CO₃-treated Cd₂Ta₂O₇ (Na-Cd-Ta₃N₅, c) crystals by nitridation at 850 °C for 20 h under an NH₃ flow, irradiated by UV (355 nm) laser pulses under a vacuum. Pump energy is 0.5 mJ/pulse, and repetition rate is 5 Hz. Insets represent expanded mid-IR regions.

tribution of the surface defects on the prolongation of the lifetimes of charge carriers [47]. Despite the fact that Cd-Ta₃N₅ with unique porous structures showed a lower photocatalytic activity for O₂ evolution compared with Na-Ta₃N₅, the studies of the effects of various cocatalysts and experimental conditions will be of research interest to further explore the potential application of stable Ta₃N₅ porous crystal structures.

4. Conclusions

In summary, the limited findings presented and discussed throughout this paper enable us to draw a preliminary conclusion that is the CdTiO_{3-x}N_y, CdNbO₂N, and CdTaO₂N phases could not be formed by applying conventional one- and two-step fabrication methods due to the low volatilization temperature of cadmium and susceptibility of titanium and niobium to reduction under high-temperature NH₃ atmosphere. The authors of the present work believe that these crystal phases may still be possible to form

by applying other synthesis techniques, including high-pressure approach [48]. Under high-temperature NH_3 atmosphere, only $\text{Cd}_2\text{Ta}_2\text{O}_7$ was fully converted to single-phase Ta_3N_5 that showed nearly four times higher O_2 evolution rate with CoO_x cocatalyst compared with its bare counterpart. An improved photocatalytic activity for O_2 evolution is related to the higher density of nucleation centers of CoO_x nanoparticles in the form of dangling bonds in porous Ta_3N_5 crystal structures and long-lived photogenerated holes, as attested by time-resolved absorption spectroscopy.

Acknowledgement

This research was supported in part by the Japan Technological Research Association of Artificial Photosynthetic Chemical Process (ARPCHEM).

Appendix A. Supplementary data

Supplementary data associated with this article can be found, in the online version, at <http://dx.doi.org/10.1016/j.apcatb.2015.10.002>.

References

- [1] N.S.P. Bhuvanesh, J. Gopalakrishnan, *J. Mater. Chem.* 7 (1997) 2297–2306.
- [2] S. Walia, S. Balendhran, H. Nili, S. Zhuyikov, G. Rosengarten, Q.H. Wang, M. Bhaskaran, M.S. Sriram, K. Kalantar-zadeh, *Prog. Mater. Sci.* 58 (2013) 1443–1489.
- [3] S.G. Ebbinghaus, H.-P. Abicht, R. Dronskowski, T. Müller, A. Reller, A. Weidenkaff, *Prog. Solid State Chem.* 37 (2009) 173–205.
- [4] M. Yang, J. Oró-Solé, J.A. Rodgers, A. Belén Jorge, A. Fuertes, J.P. Attfield, *Nat. Chem.* 3 (2011) 47–52.
- [5] P.J. Camp, A. Fuertes, J.P. Attfield, *J. Am. Chem. Soc.* 134 (2012) 6762–6766.
- [6] A. Fuertes, *J. Mater. Chem.* 22 (2012) 3293–3299.
- [7] M. Higashi, K. Domen, R. Abe, *J. Am. Chem. Soc.* 135 (2013) 10238–10241.
- [8] K. Ueda, T. Minegishi, J. Clune, M. Nakabayashi, T. Hisatomi, H. Nishiyama, M. Katayama, J. Shibata, T. Yamada, K. Domen, *J. Am. Chem. Soc.* 137 (2015) 2227–2230.
- [9] I.E. Castelli, T. Olsen, S. Datta, D.D. Landis, S. Dahl, K.S. Thygesen, K.W. Jacobsen, *Energy Environ. Sci.* 5 (2012) 5814–5819.
- [10] W. Li, E. Ionescu, R. Riedel, A. Gurlo, *J. Mater. Chem. A* 1 (2013) 12239–12245.
- [11] M. Hojamberdiev, K. Yubuta, J.J.M. Vequizo, A. Yamakata, K. Domen, S. Oishi, K. Teshima, *Cryst. Growth Des.* 15 (2015) 4663–4671.
- [12] M. Hojamberdiev, A. Yamaguchi, K. Yubuta, S. Oishi, K. Teshima, *Inorg. Chem.* 54 (2015) 3237–3244.
- [13] K. Kawashima, M. Hojamberdiev, H. Wagata, K. Yubuta, S. Oishi, K. Teshima, *Cryst. Growth Des.* 15 (2015) 333–339.
- [14] H. Moriwake, A. Kuwabara, C.A.J. Fisher, H. Taniguchi, M. Itoh, I. Tanaka, *Phys. Rev. B* 84 (2011) 104114.
- [15] N.N. Kolpakova, P. Charnetzki, W. Nawrochik, P.P. Syrnikov, A.O. Lebedev, *J. Exp. Theor. Phys.* 94 (2002) 395–402.
- [16] M. Fischer, T. Malcherek, U. Bismayer, P. Blaha, K. Schwarz, *Phys. Rev. B* 78 (2008) 014108.
- [17] D. Noureldine, D.H. Anjum, K. Takanabe, *Phys. Chem. Chem. Phys.* 16 (2014) 10762–10769.
- [18] Y. Kim, *ACS Appl. Mater. Interfaces* 4 (2012) 2329–2333.
- [19] K. Oura, V.G. Lifshits, A. Saranin, A.V. Zotov, M. Katayama, *Surface Science: An Introduction*, Springer, Berlin–Heidelberg, 2010.
- [20] J.J. De Yoreo, L.A. Zepeda-Ruiz, R.W. Friddle, S.R. Qiu, L.E. Wasylenko, A.A. Chernov, G.H. Gilmer, P.M. Dove, *Cryst. Growth Des.* 9 (2009) 5135–5144.
- [21] W.K. Burton, N. Cabrera, F.C. Frank, *Phil. Trans. R. Soc. London A* 243 (1951) 299–358.
- [22] W. Li, D. Li, X. Gao, A. Gurlo, S. Zander, P. Jones, A. Navrotsky, Z. Shen, R. Riedel, E. Ionescu, *Dalton Trans.* 44 (2015) 8238–8246.
- [23] N.-Y. Park, Y.-I. Kim, *J. Mater. Sci.* 47 (2012) 5333–5340.
- [24] A.E. Maegli, S. Pokrant, T. Hisatomi, M. Trottmann, K. Domen, A. Weidenkaff, *J. Phys. Chem. C* 118 (2014) 16344–16351.
- [25] D. Lu, G. Hitoki, E. Katou, J.N. Kondo, M. Hara, K. Domen, *Chem. Mater.* 16 (2004) 1603–1605.
- [26] X. Feng, T.J. LaTempa, J.I. Basham, O.K. Mor, C.A. Grimes, *Nano Lett.* 10 (2010) 948–952.
- [27] R. Asahi, T. Morikawa, T. Ohwaki, K. Aoki, Y. Taga, *Science* 293 (2001) 269–271.
- [28] C. Di Valentini, E. Finazzi, G. Pacchioni, A. Selloni, S. Livraghi, M.C. Paganini, E. Giamello, *Chem. Phys.* 339 (2007) 44–56.
- [29] A. Kasahara, K. Nukumizu, T. Takata, J.N. Kondo, M. Hara, H. Kobayashi, K. Domen, *J. Phys. Chem. B* 107 (2003) 791–797.
- [30] K. Kawashima, M. Hojamberdiev, H. Wagata, J.J.M. Yubuta, A. Vequizo, S. Yamakata, K. Oishi, K. Teshima, *J. Phys. Chem. C* 119 (2015) 15896–15904.
- [31] V.V. Atuchin, J.-C. Grivel, Z. Zhang, *Chem. Phys.* 360 (2009) 74–88.
- [32] W.-J. Chun, A. Ishikawa, H. Fujisawa, T. Takata, J.N. Kondo, M. Hara, M. Kawai, Y. Matsumoto, K. Domen, *J. Phys. Chem. B* 107 (2003) 1798–1803.
- [33] E. Atanassova, D. Spassov, *Appl. Surf. Sci.* 135 (1998) 71–82.
- [34] S.S.K. Ma, T. Hisatomi, K. Maeda, Y. Moriya, K. Domen, *J. Am. Chem. Soc.* 134 (2012) 19993–19996.
- [35] K. Maeda, K. Domen, *J. Phys. Chem. C* 111 (2007) 7851–7861.
- [36] A. Kudo, H. Kato, I. Tsuji, *Chem. Lett.* 33 (2004) 1534–1539.
- [37] B.A. Pinaud, P.C.K. Vesborg, T.F. Jaramillo, *J. Phys. Chem. C* 116 (2012) 15918–15924.
- [38] K. Takanabe, K. Domen, *Green* 1 (2011) 313–322.
- [39] Z. Lin, A. Orlov, R.M. Lambert, M.C. Payne, *J. Phys. Chem. B* 109 (2005) 20948–20952.
- [40] S.C. Warren, K. Voitchovsky, H. Dotan, C.M. Leroy, M. Cornuz, F. Stellacci, C. Hébert, A. Rothschild, M. Grätzel, *Nat. Mater.* 12 (2013) 842–849.
- [41] A. Dabirian, R. van de Krol, *Appl. Phys. Lett.* 102 (2013) 033905.
- [42] A.E. Maegli, S. Pokrant, T. Hisatomi, M. Trottmann, K. Domen, A. Weidenkaff, *J. Phys. Chem. C* 118 (2014) 16344–16346.
- [43] J. Feng, D. Cao, Z. Wang, W. Luo, J. Wang, Z. Li, Z. Zou, *Chem. Eur. J.* 20 (2014) 16384–16390.
- [44] A. Yamakata, T.A. Ishibashi, H. Onishi, *J. Phys. Chem. B* 105 (2001) 7258–7262.
- [45] A. Yamakata, M. Kawaguchi, N. Nishimura, T. Minegishi, J. Kubota, K. Domen, *J. Phys. Chem. C* 118 (2014) 23897–23906.
- [46] A. Yamakata, H. Yeilin, M. Kawaguchi, T. Hisatomi, J. Kubota, Y. Sakata, K. Domen, *J. Photochem. Photobiol. A* (2015), <http://dx.doi.org/10.1016/j.jphotochem.2015.05.016>.
- [47] J. Nelson, S.A. Haque, D.R. Klug, J.R. Durrant, *Phys. Rev. B* 63 (2001) 205321.
- [48] C. Tassel, Y. Kuno, Y. Goto, T. Yamamoto, C.M. Brown, J. Hester, K. Fujita, M. Higashi, R. Abe, Y. Tanaka, H. Kageyama, *Angew. Chem. Int. Ed.* 54 (2015) 516–521.